Supporting Information

Bioinspired Metal-Organic Helicate Drives Electrocatalytic Ethane Production from Carbon Dioxide

Liu Gao, Jinfeng Wang, Kesheng Shen, Xu Jing * and Chunying Duan

School of Chemistry, Dalian University of Technology, Dalian 116024, China.

Corresponding to: Xu Jing, xjing@dlut.edu.cn

Table of contents

1. Supplementary methods

Experimental Methods

Materials and Characterisation.

All substrates were used as received from commercial suppliers unless otherwise stated. Chemicals were purchased from Sigma-Aldrich, Chempur, TCI, or Alfa Aesar. Carbon dioxide (99.995%) was purchased from the Dalian Institute of Special Gases and used as received. Electrocatalytic systems such as electrochemical cells (H-cell and flow cell) were purchased from Gaossunion.

^{1}H-NMR and ^{13}C-NMR spectra were measured on a Bruker 400 and 500 MHz spectrometer (in DMSO-d_6 or D_2O, 1,3,5-trimethoxybenzene as the internal standard). Diffusion-ordered spectroscopy (^{1}H-DOSY) spectra were measured on a Bruker 400 MHz spectrometer (in DMSO-d_6). Electrospray ionization mass spectrometry (ESI-MS) spectra were obtained using an HPLC-ESI-TOF/MS Agilent G6224A mass spectrometer with acetonitrile as the mobile phase.

Single crystal X-ray diffraction data collection was performed using a Bruker D8 VENTURE Metaljet PHOTON II diffractometer with a Ga-Kα (λ =1.34138 Å) radiation at 185 K. The structure was solved by direct methods and refined on F^2 by full-matrix least-squares methods with Olex 2 version 1.2 software.

UV-Vis spectra were measured on a UV-2600 spectrometer. The solution fluorescent spectra were measured on an Edinburgh FS-920 instrument. Isothermal Titration Calorimetry (ITC) was performed on a Nano ITC (TA Instruments Inc. Waters LLC). The gas product produced by electrocatalysis was characterized by SHIMADZU GC-2014 gas chromatographic analysis.

Electrochemical measurements were performed using a CHI 760E workstations with an Ag/AgCl electrode as a reference electrode, a platinum wire with a 1.0 mm diameter as a counter electrode, and a glassy carbon or hydrophobic carbon paper electrode as a working electrode. *In situ* laser confocal Raman spectra were measured on a LabRAM HR Evolution spectrometer.

Electrochemical Experimental Test Methods

The electro-chemical experimental tests were carried out in a custom-made two chamber H-type cell on a CHI 760E workstation with the hydrophobic carbon paper as the working electrode, Ag/AgCl electrode with a 3 M KCl solution as the reference, platinum sheet (5.0 mm diameter) as the counter electrode. A proton exchange membrane (Nafion N117) separated the two chambers of the H-cell. After each experiment, the proton exchange membrane should be refluxed in dilute H_2O_2 and H_2SO_4 for 0.5-3 hours, respectively.

During the electrochemical tests, the cathodic chamber of the H-cell was filled with 30 mL CH_3CN/H_2O (v/v = 2:1), 0.1 M $LiClO_4$, 1.5 M PZ, room temperature (standard conditions).Wherein, 0.01 mM **H1** catalysts were added to the cathode cell, CO_2 (or simulated

flue gas or Ar (99.999%) for blank experiments) was bubbled through the electrolyte in the working electrode chamber with a flow rate of 10 standard cubic centimeters per minute until the solution pH=8.0. Another, anodic chamber of the H-cell was filled with 30 mL CH_3CN/H_2O (v/v = 2:1), 0.1 M $LiClO_4$ and 5.0 mM QHQ. Ar was bubbled through the electrolyte in the anodic chamber with a flow rate of 10 standard cubic centimeters per minute for at least 40 minutes to remove oxygen before the tests. The cathode gas outlet is introduced into the gas sampling loop of the gas chromatograph for quantitative analysis of C_2H_6, C_2H_4 and H_2.

Synthesis section

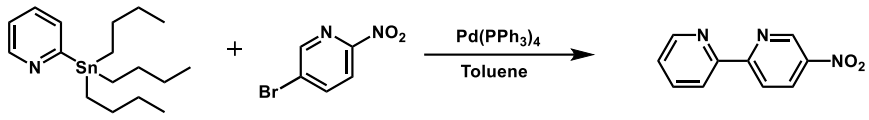

Synthesis of **5-Nitroo-2,2'-bipyridine**:[1] A mixture of 2-Bromo-5-nitropyridine (3.6 g, 17.74 mmol), 200 mL anhydrous toluene and 2-(tributylstannyl) pyridine (4.7 mL, 14.58 mmol) was degassed with argon for 20 min, $Pd(PPh_3)_4$ (0.87 g, 0. 75 mmol) was added into the mixture. The reaction mixture was degassed and heated to reflux under argon for 3 days, then cooled to room temperature. The precipitated residue was filtered off, and the filtrate was extracted with DCM, dried over $MgSO_4$ and subsequently evaporated under vacuum. The residue was purified by silica gel column chromatography (Petroleum ether/Ethyl acetate v/v = 4:1), then the precipitate was dried in a vacuum to obtain the powdered product without further purification. Yield: 55%. ^{1}H NMR (500 MHz, DMSO-d_6, ppm, 298 K): δ 9.46 (s, 1H), 8.82-8.70 (m, 2H), 8.62 (d, J=8.7 Hz, 1H), 8.47 (d, J=7.8 Hz, 1H), 8.09-7.98 (m, 1H), 7.64-7.53 (m, 1H).

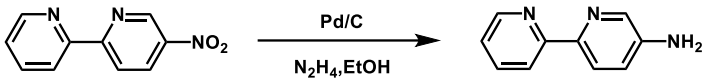

Synthesis of **5-Amino-2,2'-bipyridine**:[2] Add 5-Nitroo-2,2'-bipyridine (1.07 g,5.3 mmol), Pd/C (0.25 g, 2.34 mmol) and 100 mL ethanol into a 250 mL double-necked flask, and pass in argon. After heating to reflux, slowly add 20 mL of hydrazine hydrate with a constant pressure ground liquid funnel, reflux and stir for 24 hours. After cooling, filter with diatomaceous earth as a filter aid, then add the filtrate to ice water and filter again to collect it. The precipitate was dried in a vacuum at room temperature to obtain a white powder product. Yield: 95%. ^{1}H NMR (500 MHz, DMSO-d_6, ppm, 298 K): δ 8.54 (d, J=4.9 Hz, 1H), 8.18 (d, J=8.0 Hz, 1H), 8.08 (d, J=8.5 Hz, 1H), 8.03 (d, J=2.8 Hz, 1H), 7.84-7.75 (m, 1H), 7.25 (dd, J=7.5, 4.7 Hz, 1H), 7.03 (dd, J=8.5, 2.9 Hz, 1H), 5.69 (s, 2H).

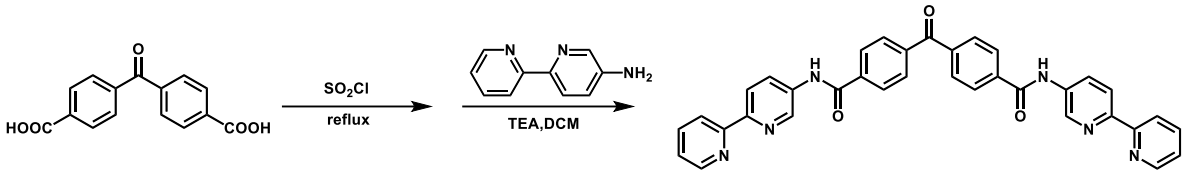

Synthesis of **4,4'-carbonylbis(N-([2,2'-bipyridin]-5-yl)benzamide)**: Under the anhydrous atmosphere, 4,4'-carbonyldibenzoic acid (0.405 g, 1.5 mmol) in $SOCl_2$ (15 mL) was stirred at 80 ℃ for 12 h. The reaction vessel was cooled to room temperature and the solvents were removed under vacuum. The resulting solid was then dissolved in anhydrous DCM (30 mL), which was gradually added to a solution of 5-Amino-2,2'-bipyridine (0.52 g, 3.05 mmol), triethylamine (3 mL) in anhydrous DCM (30 mL). The suspension was stirred at room temperature for 4 days. Then the precipitate was collected, washed with water, DCM. Subsequent drying under high vacuum led to L as a pale yellow solid. Yield: 60%.^{1}H NMR (500 MHz, DMSO-d_6, ppm, 298 K) δ 10.88 (s, 2H), 9.09 (dd, J = 2.3, 1.1 Hz, 2H), 8.68 (ddd, J = 4.8, 1.8, 0.9 Hz, 2H), 8.47-8.39 (m, 4H), 8.37 (dt, J = 8.0, 1.2 Hz, 2H), 8.22-8.15 (m, 4H), 8.01-7.90 (m, 6H), 7.44 (ddd, J = 7.5, 4.8, 1.2 Hz, 2H).

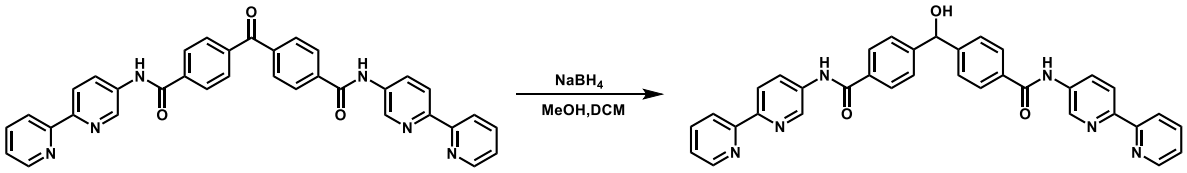

Synthesis of 4,4'-(hydroxymethylene)bis(N-([2,2'-bipyridin]-5-yl)benzamide)(Ligand **L**):[3] A mixture of MeOH (20 ml), anhydrous DCM (10mL), NaBH4(0.38g, 10 mmo) and 4,4'-carbonylbis(N-([2,2'-bipyridin]-5-yl)benzamide) (0.576 g, 1.0 mmol) was stirred in a two neck round bottom flask for 6 hours. After the indicated time, concentrated HCl was added to the mixture to adjust the pH to 1, and the precipitated solid was filtered, washed with water and methanol and filtered to get the desired product. Yield: 80%.^{1}H NMR (500 MHz, DMSO-d_6, ppm, 298 K) δ 10.58 (s, 2H), 9.04 (d, J = 2.4 Hz, 2H), 8.67 (dt, J = 4.7, 1.3 Hz, 2H), 8.44-8.25 (m, 6H), 8.01-7.88 (m, 6H), 7.62 (d, J = 8.1 Hz, 4H), 7.42 (ddd, J = 7.5, 4.8, 1.2 Hz, 2H), 6.29 (d, J = 4.0 Hz, 1H), 5.94 (d, J = 4.0 Hz, 1H). ^{13}C NMR (101 MHz, DMSO-d_6 ppm, 298 K) δ 166.32, 155.51, 150.71, 149.68, 141.63, 137.70, 136.82, 133.48, 128.34, 128.28, 126.69, 120.90, 120.47.

Synthesis of the single crystal **H1 (ClO_4^-)**: Ligand **L** (57.8 mg, 0.1 mmol) and iron (II) perchlorate (11.0 mg, 0.07 mmol) were dissolved in 20 mL anhydrous DMF. The mixture was stirred and refluxed for 8 h under an inert gas. Then the supernatant was filtered twice with a filter, 2 mL of solution was added to a 20 mL tube, and sealed with a plastic film and raw tape. All tubes were placed in a wide-mouth bottle, and 150-200 mL of ether was added. The bottle was sealed and the crystal was obtained by static growth at room temperature for 3 weeks. Yield: 45%. HRMS (ESI) m/z calc. for $[Fe_2L_3]^{4+}$ 461.8727, found: 461.8786; $[Fe_2L_3\text{-}H^+]^{3+}$ 615.4945, found: 615.5005; $[Fe_2L_3+ClO_4^-]^{3+}$ 648.8133, found: 648.8190; $[Fe_2L_3\text{-}2H^+]^{3+}$ 922.2345, found: 922.2365; $[Fe_2L_3+ClO_4^-\text{-}H^+]^{2+}$ 973.0728, found: 973.0734; $[Fe_2L_3+2ClO_4^-]^{2+}$ 1023.1903, found: 1023.1937.

Synthesis of the single crystal **H2 (BF_4^-)**: Ligand **L** (57.8 mg, 0.1 mmol) and iron (II) tetrafluoroborate (16.5 mg, 0.07 mmol) were dissolved in 20 mL anhydrous DMF. The mixture was stirred and refluxed for 8 h under an inert gas. Then the supernatant was filtered twice with a filter, 2 mL of solution was added to a 20 mL tube, and sealed with a plastic film and raw tape. All tubes were placed in a wide-mouth bottle, and 150-200 mL of ether was added. The bottle was sealed and the crystal was obtained by static growth at room temperature for 3 weeks. Yield: 50%.

Synthesis of the mononuclear iron complex **M1**: Dissolve 2,2'-bipyridine (23.4 mg, 0.15 mmol) and iron(II) trifluoromethanesulfonate (17.7 mg, 0.05 mmol) in 25 mL of anhydrous methanol and reflux for 24 hours under argon. Transfer 2 mL of the solution to a 20 mL test tube and seal with plastic wrap and PTFE tape. Place the tube in a wide-mouth flask, add 150 mL of ether and seal. After being left in the dark for two weeks, crystals were obtained. Yield: 90%. HRMS (ESI) m/z calc. for $[Fe(bpy)_3]^{2+}$ 262.0705, found: 262.0707.

Experimental parameter computational formulas

Calculations of faradaic efficiencies of gaseous products[4]: The gas products were collected by using the 5 mL injector without air, and then injected into gas chromatography. The Faradaic efficiency (FE) of gaseous product is:

$$FE = \frac{n\ N\ F}{Q} \times 100\%$$

Q: the charge obtained from the test during CO_2 reduction (C), F: faradaic constant (96485 C/mol), N: the number of electrons required to generate the product, n: the moles of products (mol). For the product of H_2, CO, C_2H_4 and C_2H_6 the N are 2, 2,12 and 14, respectively.

Calculations of TON, TOF and Selectivity of products[5]:

The turnover number was calculated by the equation:

$$TON = \frac{n_{pro.}}{n_{cat.}}$$

$n_{pro.}$ represents the amounts of the product (mol), $n_{cat.}$ represents the amounts of catalyst (mol).

The turnover efficiency was calculated by the equation:

$$TOF = \frac{TON}{t}$$

TON represents the turnover number, t represents the time of the reaction (h).

Stokes-Einstein equation[2]:

The Stokes-Einstein equation quantitatively describes the relationship between the self-diffusion coefficient D and its motion resistance in the fluid. When the self-diffusion coefficient of a given molecular species is known, the effective size or weight information can be obtained under controlled conditions through this equation, in which k_b is the Boltzmann constant (1.380649×10^{-23} J K^{-1}), T is the absolute temperature (298.15 K), d is the hydrodynamic diameter, the viscosity η of DMSO-d_6 is 1.987 mPa s at 298.15 K.

$$D = \frac{k_b T}{3\Pi\eta d}$$

The self-diffusion coefficient of **H1** was 1.984×10^{-10} $m^2\cdot s^{-1}$ in DMSO-d_6 solution.

Nonlinear fitting of host-guest (H-G) complex system:[6]

For a 1:1 encapsulation process:

$$H + G \rightleftharpoons HG$$

$$Y = Y_H[H]_0 + (Y_{HG} - Y_H)[HG]$$

$$\Delta Y = Y_{\Delta HG}(1 + K_a[G] + K_a[H]_0 - ((1 + K_a[G] + K_a[H]_0)^2 - 4K_a^2[H]_0[G])^{0.5})/(2K_a[H]_0)$$

$[H]_0$ is the initial concentration of the host; $[G]_0$ is the total concentration of the guest; [HG] is the concentration of the 1:1 complex of the host and guest; $[G]$ is the concentration of the guest during titration; ΔY is the physical change. The association constant K_a was obtained by non-linear regression of the obtained data.

2. Single crystal X-ray crystallography

Table S1. Single Crystal X-ray Crystallography for **H2**.

Compound	Fe_2L_3 (**H2**)
CCDC number	2527706
Formula	$Fe_2(C_{35}N_6O_3H_{26})_3$ $(C_3H_7NO)_4(BF_4)_4$
M_r (g/mol)	2487.3600
Crystal system	Triclinic
Space group	*P-1*
a (Å)	18.370(3)
b (Å)	21.463(3)
c (Å)	24.249(4)
α (°)	105.195(7)
β (°)	110.112(6)
γ (°)	96.793(7)
Volume ($Å^3$)	8432(12)
Z	2
D_{calcd} ($g/cm^{3)}$	0.945
μ (Ga-Kα, mm^{-1})	1.34138
F(000)	2482.0
T (K)	185
Rint	0.1547
wR_2 (all data)	0.2931
R_1 [$I > 2\sigma(I)$]	0.1203
Goodness of fit	1.051

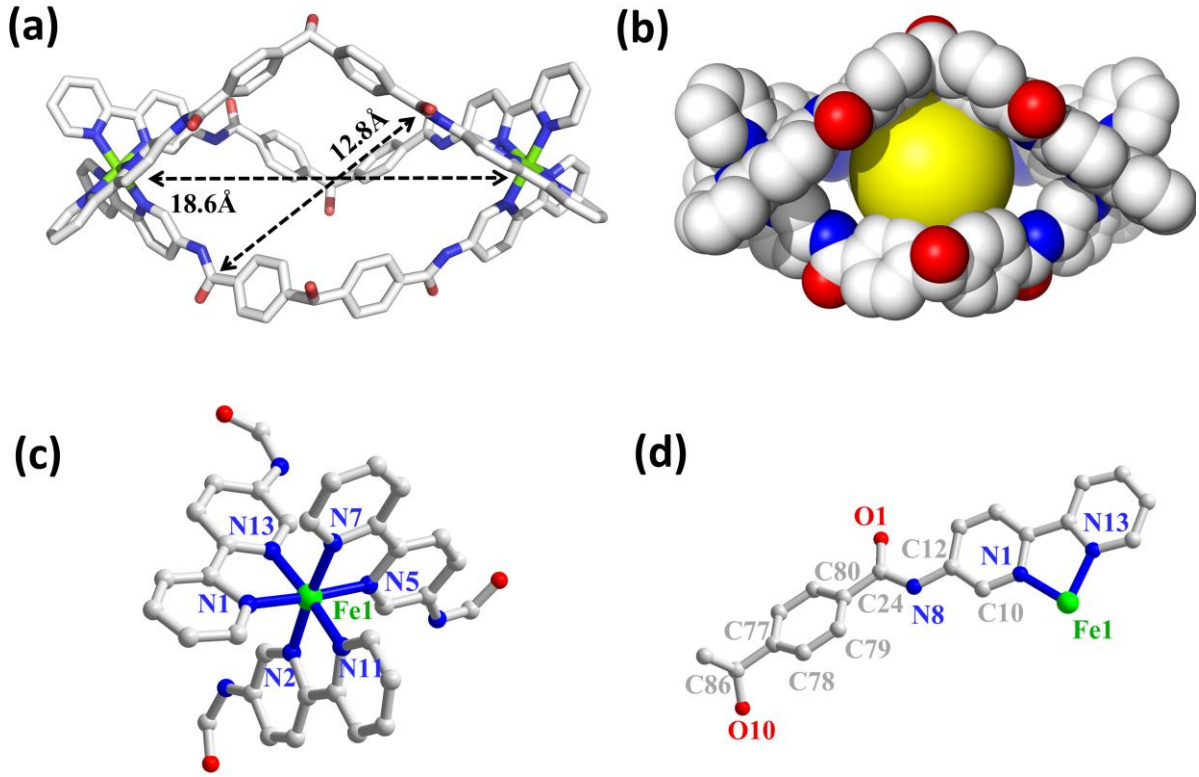

Figure S1. The crystal structure of **H2.** (a) The structure of metal-organic capsules **H2**. Fe, green; N, blue; O, red and C, gray. Hydrogen atoms, anions, and solvent molecules were omitted for clarity. (b) The space-filling pattern of **H2** shows the confined space and the opening channels. (c) Partial enlarged structure of the coordination environment of **H2**, showing the coordination geometries of the iron ions. (d) Molecular structure of **H2** capsule within a unique asymmetric unit, showing the backbone of the ligand in the complex. See tables S2 and S3 for details.

Table S2. Selective bond distance (Å) for **H2**.

Atom-Atom	Length (Å)
Fe1–N1	1.965(4)
Fe1–N2	1.954(4)
Fe1–N5	1.970(4)
Fe1–N7	1.948(5)
Fe1–N11	1.964(4)
Fe1–N13	1.954(4)
N1–C10	1.343(6)
N8-C12	1.409(7)
N8-C24	1.380(6)
O1-C24	1.246(6)
C10–C12	1.385 (7)
C24–C80	1.493(6)
C79–C80	1.390(4)
C78–C79	1.390(5)
C77–C78	1.390(4)
C77–C86	1.513(7)
C86–O10	1.365(9)

Table S3. Selective bond angle (°) for **H2**.

Atom-Atom-Atom	Bond angle (°)
N1–Fe1–N5	96.00(17)
N2–Fe1–N1	95.18(16)
N2–Fe1–N5	95.47(17)
N2–Fe1–N11	81.60(19)
N7–Fe1–N1	88.01(18)
N7–Fe1–N2	175.76(17)
N7–Fe1–N5	81.39(19)
N7–Fe1–N11	95.4(2)
N7–Fe1–N13	93.7(2)
N11–Fe1–N1	174.7(2)
N11–Fe1–N5	88.54(17)
N13–Fe1–N1	81.75(17)
N13–Fe1–N2	89.51(19)
N13–Fe1–N5	174.7(2)
N13–Fe1–N11	93.96(18)
C10–N1–Fe1	127.6(3)
N1–C10–C12	123.2(5)
C10–C12–N8	116.9(4)
C12–N8–C24	126.1(4)
O1–C24–N8	121.5(5)
O1–C24–C80	121.3(5)
C24–C80–C79	123.0(3)
C78–C79–C80	120.0(2)
C77–C78–C79	120.0(3)
C78–C77–C86	118.8(4)
O10–C86–C77	113.4(6)

3. Characterization of Catalyst H1 and mononuclear complexes

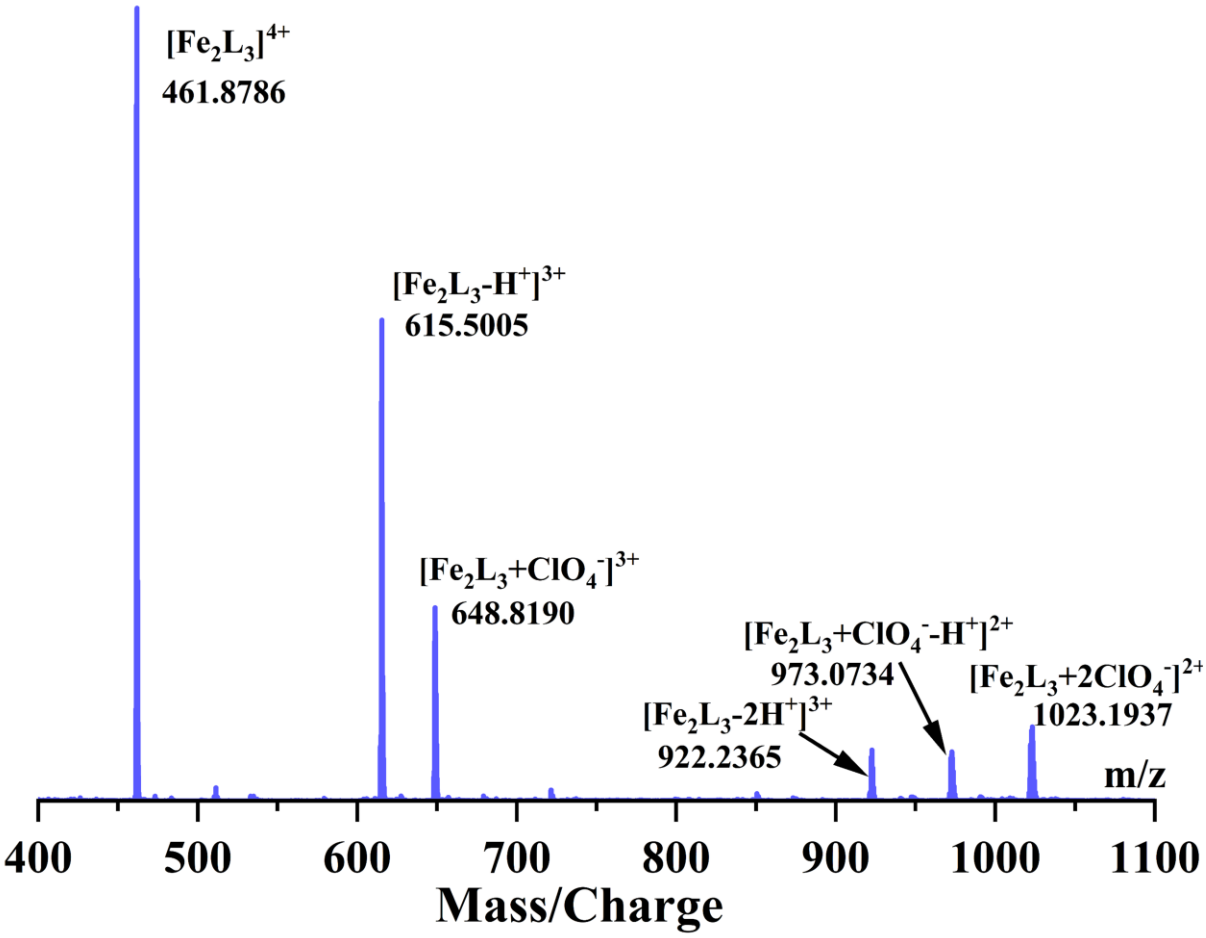

Peak	Value of m/z	Specie assigned
1	461.8786	$[Fe_2L_3]^{4+}$
2	615.5005	$[Fe_2L_3\text{-}H^+]^{3+}$
3	648.8190	$[Fe_2L_3\text{+}ClO_4^-]^{3+}$
4	922.2365	$[Fe_2L_3\text{-}2H^+]^{3+}$
5	973.0734	$[Fe_2L_3\text{+}ClO_4^-\text{-}H^+]^{2+}$
6	1023.1937	$[Fe_2L_3\text{+}2ClO_4^-]^{2+}$

Figure S2. ESI-MS spectra of **H1** in acetonitrile solution. The table shows attribution of peaks.

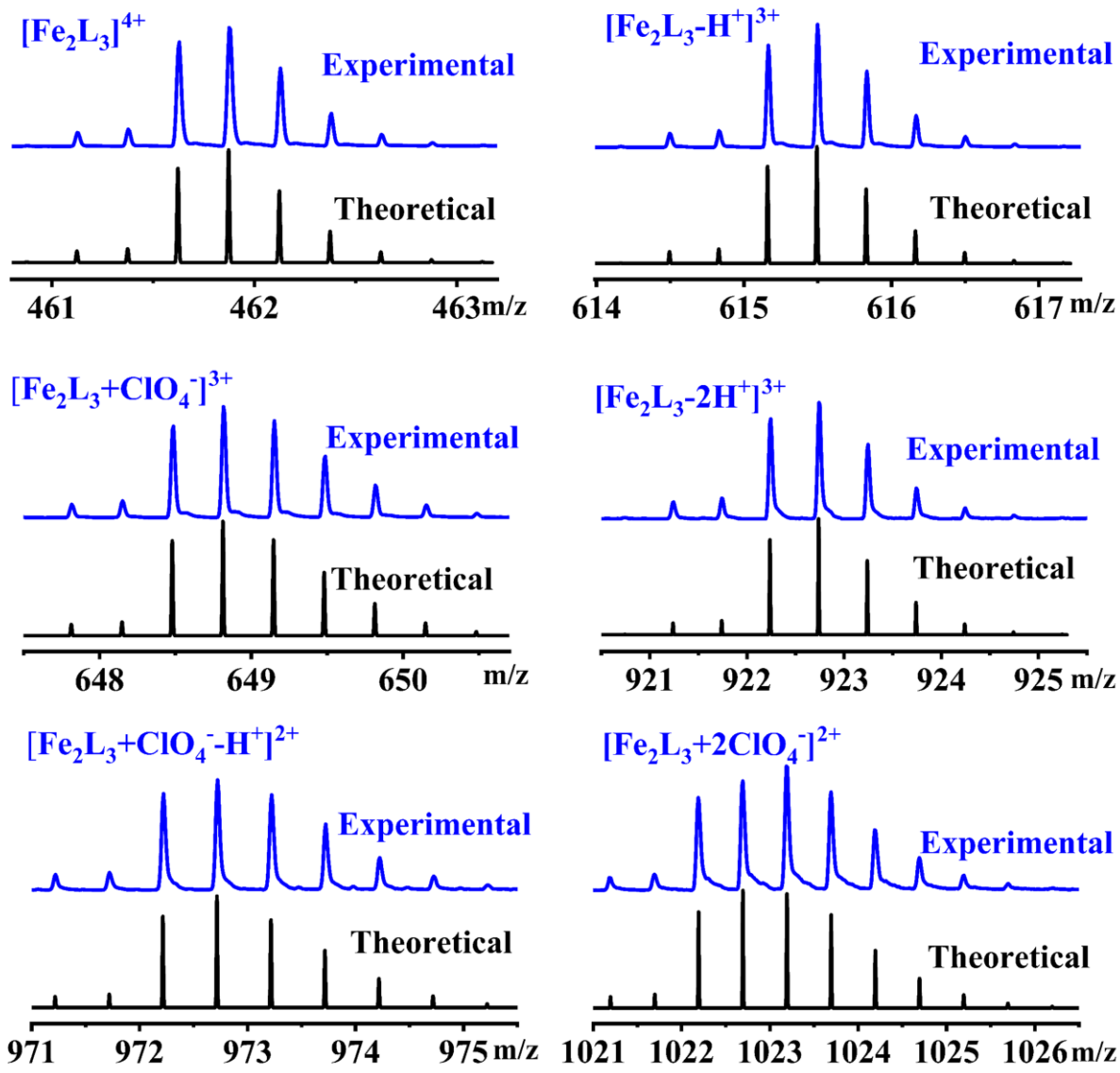

Figure S3. ESI-MS spectra of **H1** in acetonitrile solution. The figure represents the measured and simulated isotopic patterns at m/z =461.8786,615.5005,648.8190,922.2365, 973.0734, 1023.1937. $[Fe_2L_3]^{4+}$ 461.8727, found: 461.8786; $[Fe_2L_3\text{-}H^+]^{3+}$ 615.4945, found: 615.5005; $[Fe_2L_3+ClO_4^-]^{3+}$ 648.8133, found: 648.8190; $[Fe_2L_3\text{-}2H^+]^{3+}$ 922.2345, found: 922.2365; $[Fe_2L_3+ClO_4^-\text{-}H^+]^{2+}$ 973.0728, found: 973.0734; $[Fe_2L_3+2ClO_4^-]^{2+}$ 1023.1903, found: 1023.1937.

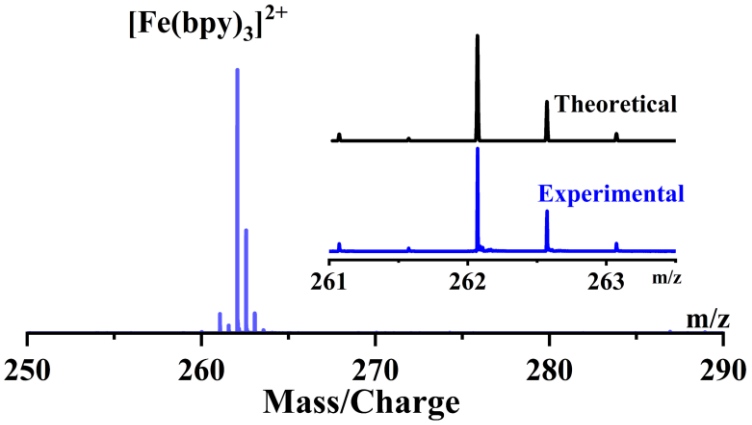

Figure S4. ESI-MS spectra of **M1** in acetonitrile solution. The inserts showed the measured and simulated isotopic patterns at m/z =262.0707.

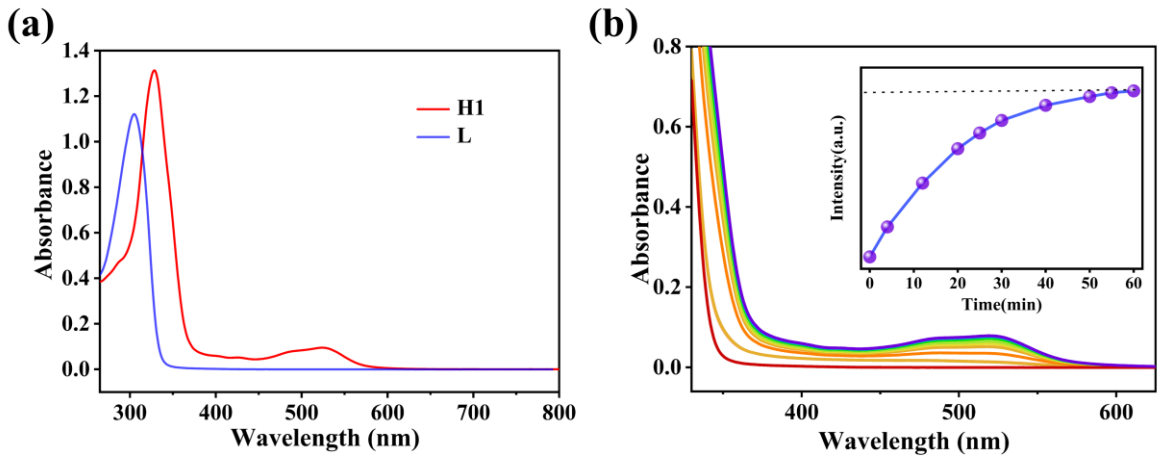

Figure S5. (a) UV-Vis absorption spectra in CH_3CN solution containing **H1** (8.0 μM) and ligand **L** (10.0 μM), respectively. (b) Time-dependent UV-Vis of the CH_3CN/H_2O (v/v = 2:1) solution containing **L** (10.0 μM) and $Fe(ClO_4)_2$ (7.0 μM). Inset: the time-dependent intensity variation at 523 nm within 60 min.

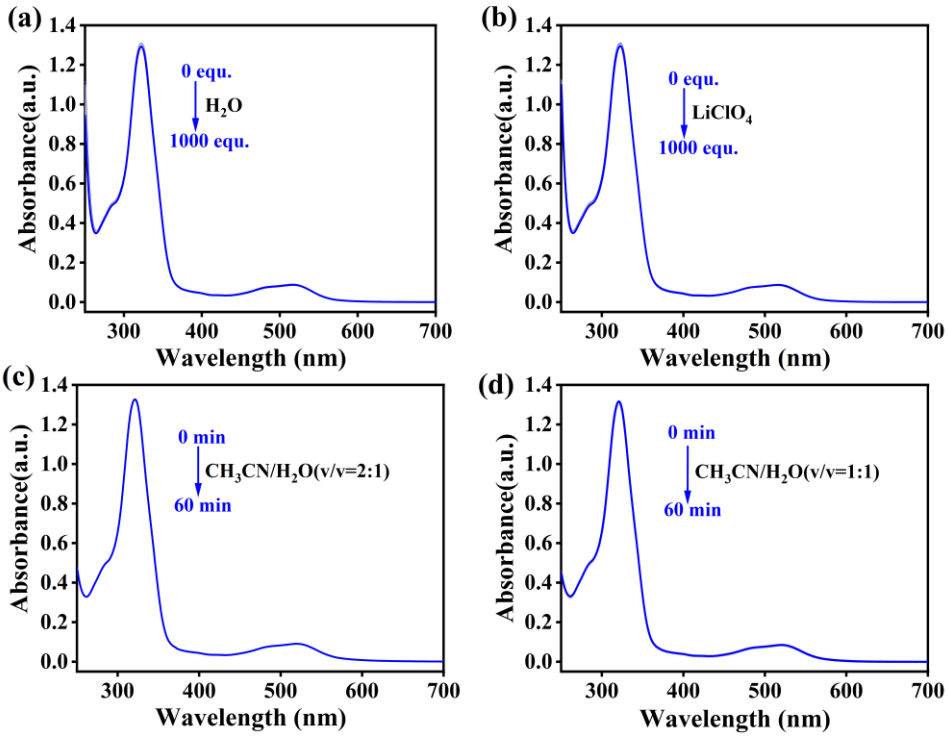

Figure S6. (a) UV-Vis absorption spectra of **H1** (8.0 μM) in CH_3CN upon the addition of (a) H_2O and (b) $LiClO_4$ (CH_3CN). UV-Vis absorption spectra of **H1** (8.0 μM) in (c) CH_3CN/H_2O (v/v=2:1) and (d) CH_3CN/H_2O (v/v=1:1) at different times. **H1** can exist stably under these conditions.

5. Interaction of host-guest.

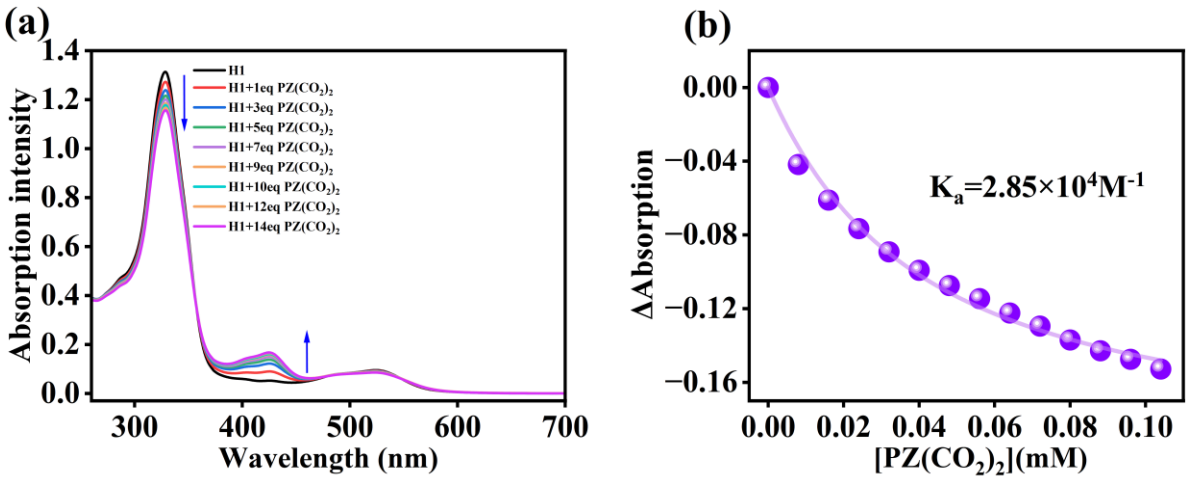

Figure S7. UV-Vis titration experiments of **H1** and $PZ(CO_2)_2$. (a) UV-Vis absorption spectra of **H1** (8.0 μM) in CH_3CN/H_2O (v/v = 2:1) solution upon the addition of $PZ(CO_2)_2$. (b) Plot of the absorbance changes at 327 nm with a nonlinear curve fitting between **H1** and $PZ(CO_2)_2$ with an associated constant calculated as 2.85×10^4 M^{-1} (1:1 binding model).

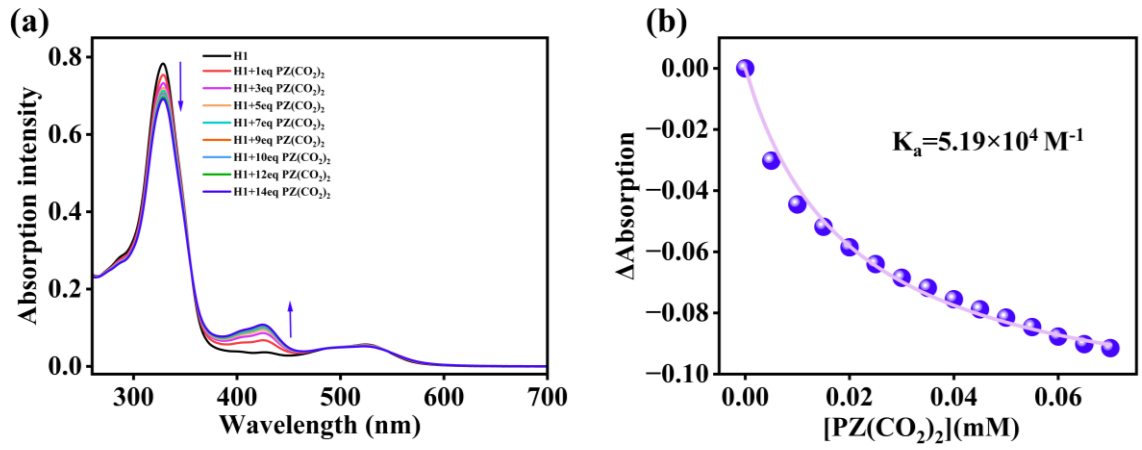

Figure S8. UV-Vis titration experiments of **H1** and $PZ(CO_2)_2$ in DMSO/H_2O (v/v = 2:1) solution. (a) UV-Vis absorption spectra of **H1** (5.0 μM) upon the addition of $PZ(CO_2)_2$. (b) Plot of the absorbance changes at 327 nm with a nonlinear curve fitting between **H1** and $PZ(CO_2)_2$ with an associated constant calculated as 5.19×10^4 M^{-1} (1:1 binding model).

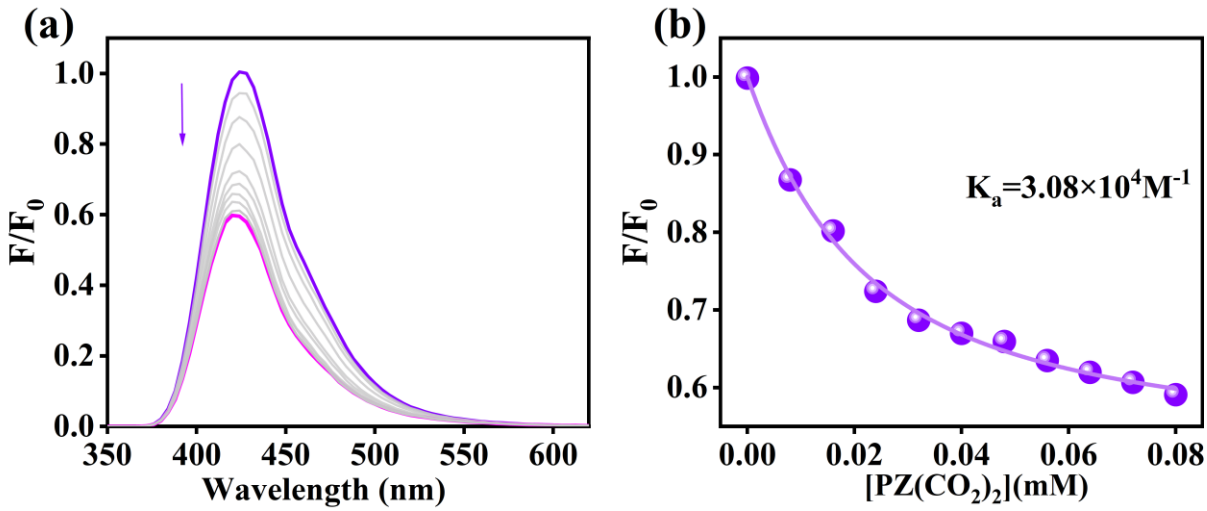

Figure S9. Fluorescence titration experiments of **H1** and $PZ(CO_2)_2$. (a) Luminescence spectra in CH_3CN/H_2O (v/v = 2:1) solution containing 8.0 μM **H1** upon addition of $PZ(CO_2)_2$. (b) Plot of the intensity changes at 428 nm with a nonlinear curve fitting between **H1** and $PZ(CO_2)_2$ with an associated constant calculated as 3.08×10^4 M^{-1} (1:1 binding model).

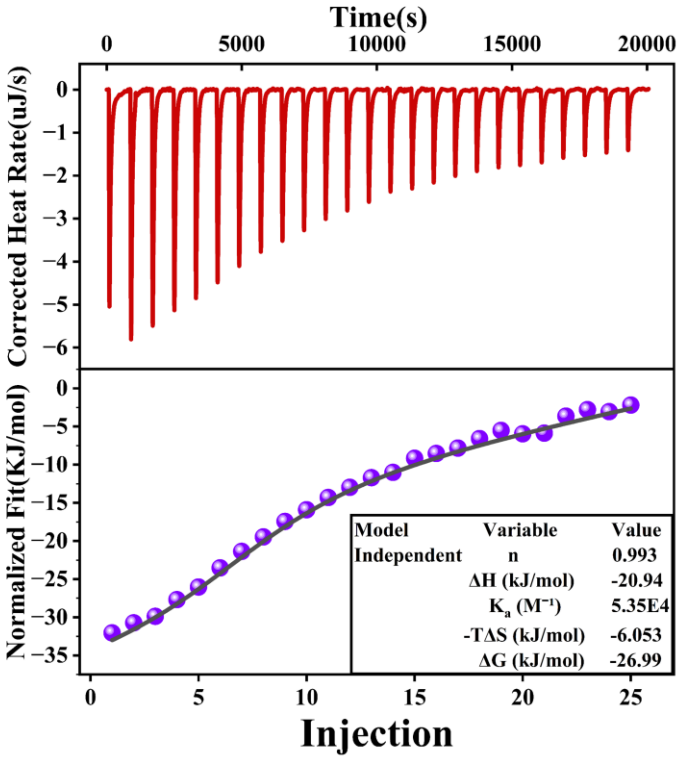

Figure S10. ITC titration experiments of **H1** and $PZ(CO_2)_2$. Microcalorimetric titration of **H1** and $PZ(CO_2)_2$ in degassed DMSO/H_2O (v/v = 2:1) solution. (top) Raw data for sequential 25 injections (8 μL per injection) of $PZ(CO_2)_2$ (3.0 mM in (DMSO/H2O v/v = 2:1) solution injected into **H1** (0.3 mM) solution. (bottom) Apparent reaction heat obtained from the integration of calorimetric traces. The titration curve showing a 1:1 host−guest behavior between **H1** and $PZ(CO_2)_2$ with an associated constant calculated as 5.35×10^4 M^{-1}.

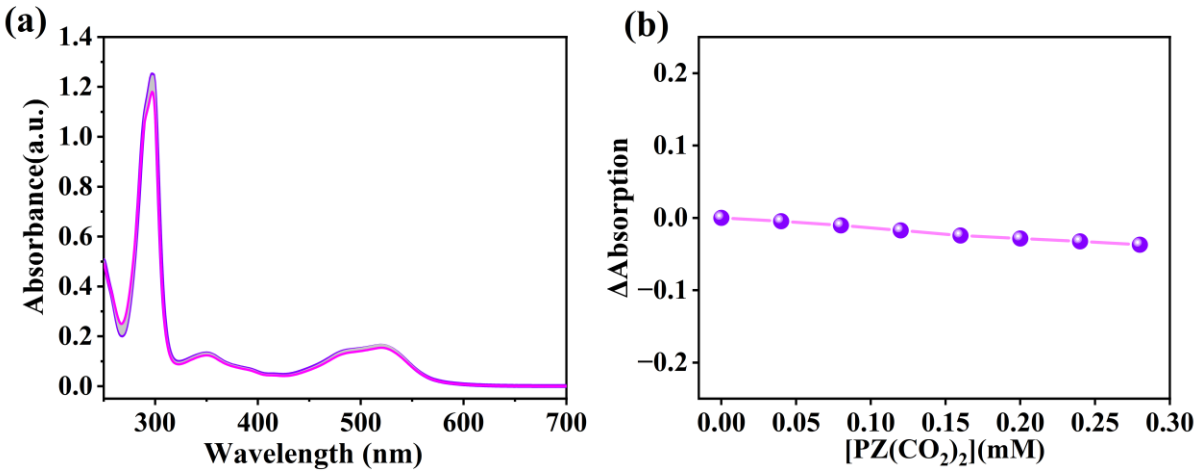

Figure S11. UV-Vis titration experiments of **M1** and $PZ(CO_2)_2$. (a) UV-Vis absorption difference spectra in CH_3CN/H_2O (v/v = 2:1) solution containing **M1** (0.01 mM) upon addition of $PZ(CO_2)_2$. (b) Plot of the absorbance changes at 297 nm, there was no obvious spectral change with the increase of $PZ(CO_2)_2$ concentration.

6. Electrochemical experiments.

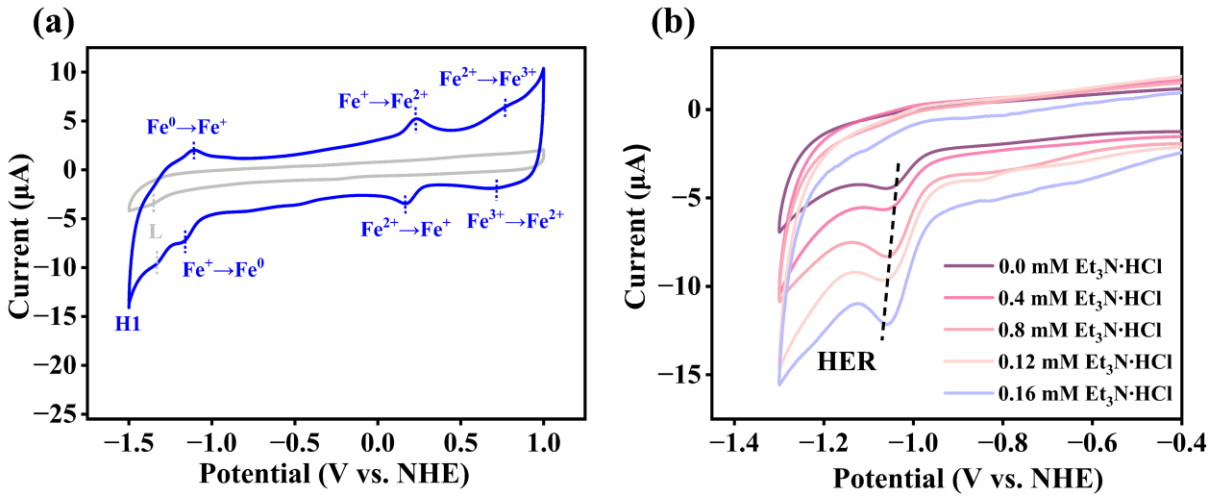

Figure S12. Cyclic voltammetry curves. (a) CV curves of 0.1 mM **L** and 0.1 mM **H1** in DMSO containing 0.1 M $LiClO_4$, respectively. (b) CV curves of the electrocatalytic HER potential in DMSO containing 0.1 M $LiClO_4$ upon the addition of different concentration of $Et_3N{\cdot}HCl$.

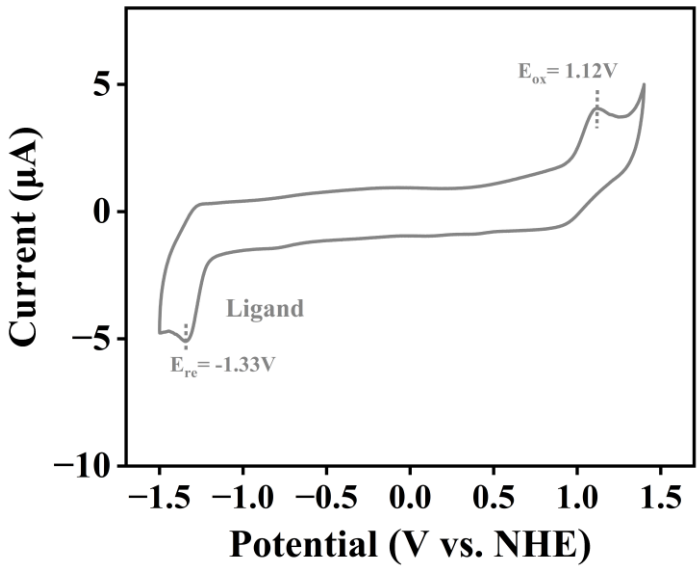

Figure S13. Cyclic voltammetry curves. CV curves of 0.1 mM **L** in CH_3CN containing 0.1 M $LiClO_4$.

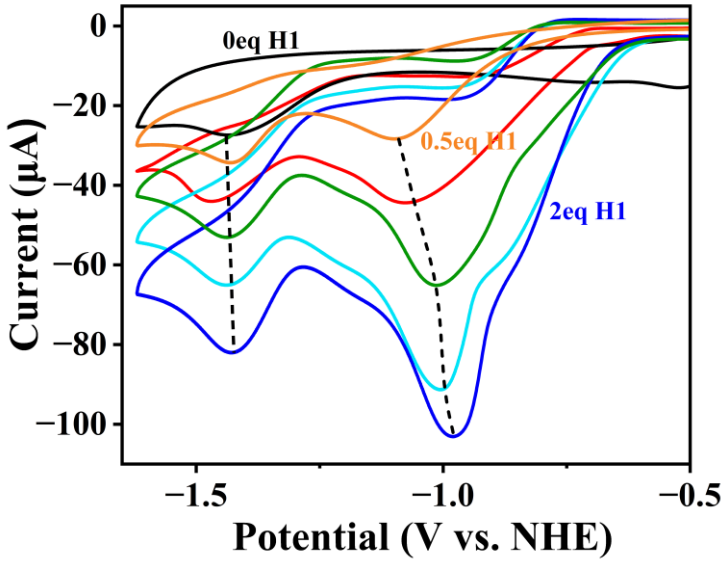

Figure S14. CV tests of electro-activation of $PZ(CO_2)_2$ by **H1**. Cyclic voltammograms of 0.1mM $PZ(CO_2)_2$ in CH_3CN (0.1 M $LiClO_4$) upon the addition of **H1** with increasing concentrations.

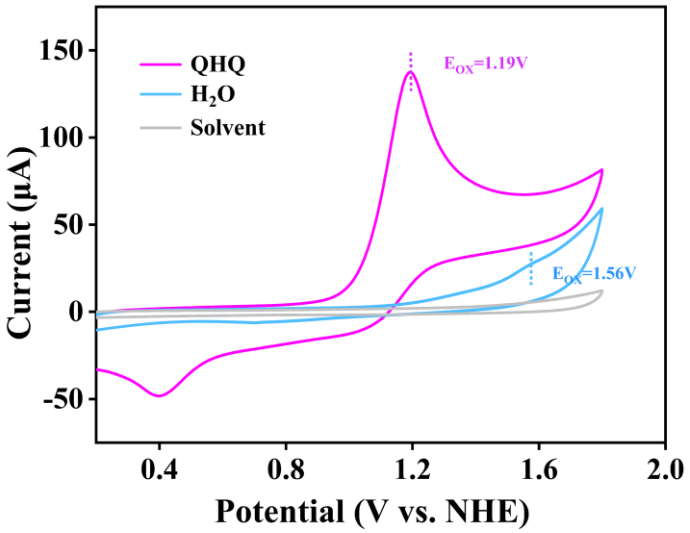

Figure S15. CV tests of anodic oxidation potential. CV curves of the H_2O (1.0 mM) and QHQ (1.0 mM) in CH_3CN containing 0.1 M $LiClO_4$ at 0.05 $V \cdot s^{-1}$ scan rate. The oxidation potential of QHQ is 1.19 V vs. NHE, and the oxidation potential of H_2O is 1.56 V vs. NHE.

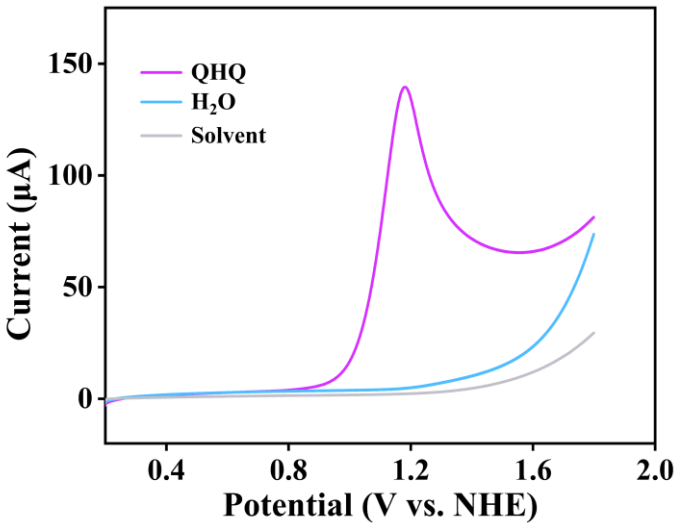

Figure S16. LSV tests of anodic oxidation potential. LSV curves of the QHQ (1.0 mM) and H_2O (1.0 mM) in CH_3CN containing 0.1 M $LiClO_4$ at 0.05 $V \cdot s^{-1}$ scan rate.

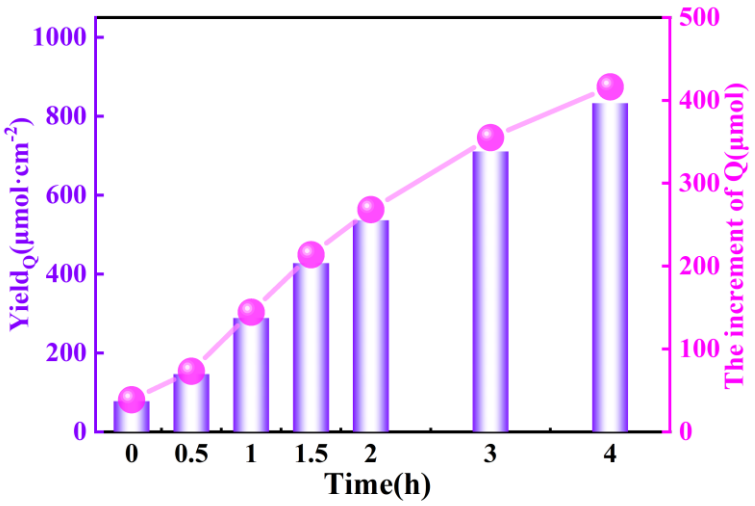

Figure S17. Distribution of hydroquinone oxidation products at the anode at different times under a cathode potential of -0.53 V vs. RHE.

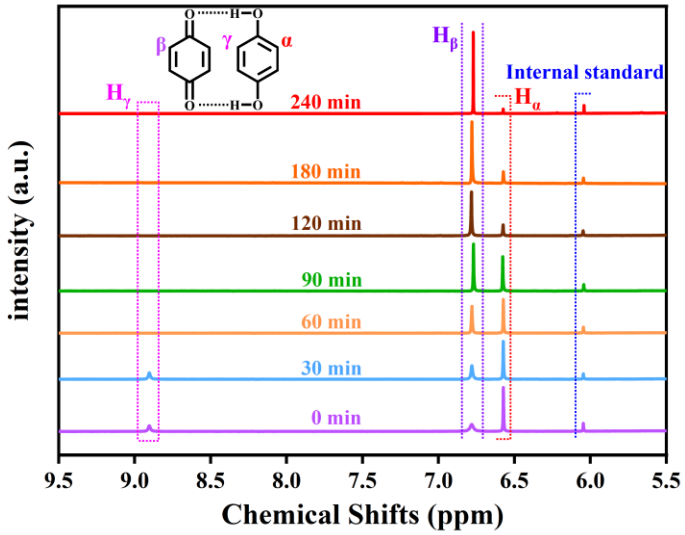

Figure S18. ^{1}H NMR spectra of hydroquinone oxidation products of anode at different times under cathode potential -0.53 V vs. RHE. 1,3,5-trimethoxybenzene was used as internal standard. (500 MHz, 298 K).

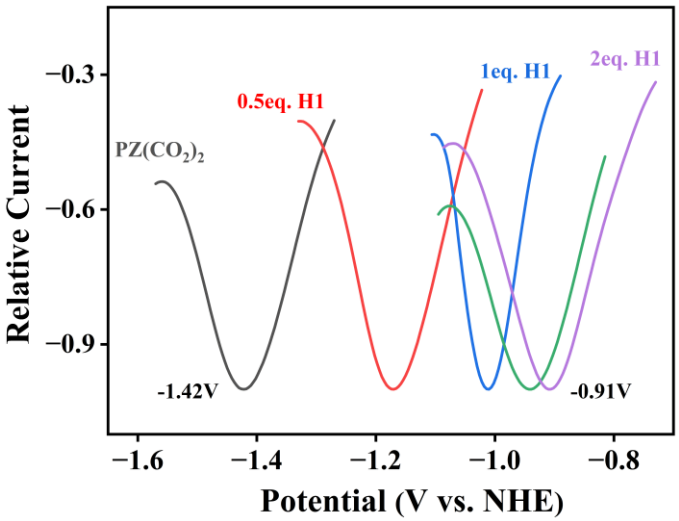

Figure S19. Electrochemical titration experiments of **H1** and $PZ(CO_2)_2$. The DPV curves of 0 eq.~ 2.0 eq. **H1** in CH_3CN /H_2O (v/v = 2:1) containing 0.1 M $LiClO_4$ with $PZ(CO_2)_2$ (0.1 mM).

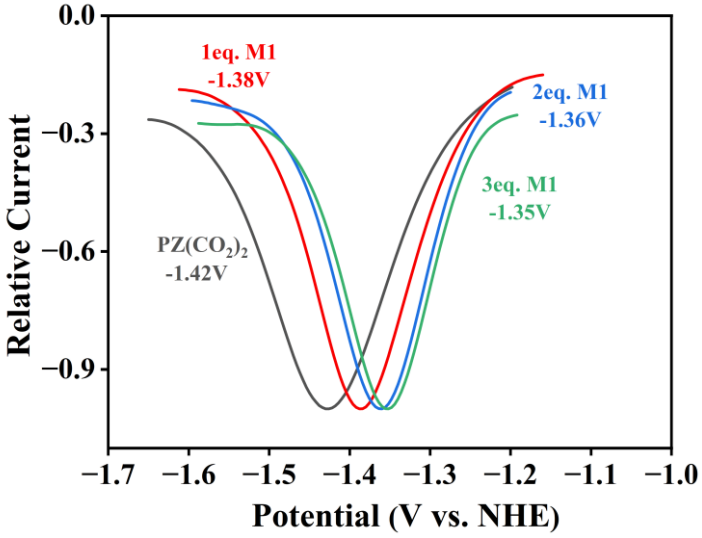

Figure S20. Electrochemical titration experiments of **M1** and $PZ(CO_2)_2$. The DPV curves of 0 eq.~ 3.0 eq. **M1** in CH_3CN /H_2O (v/v = 2:1) containing 0.1 M $LiClO_4$ with $PZ(CO_2)_2$ (0.1 mM). There were no obvious shifts with the increase of **M1**.

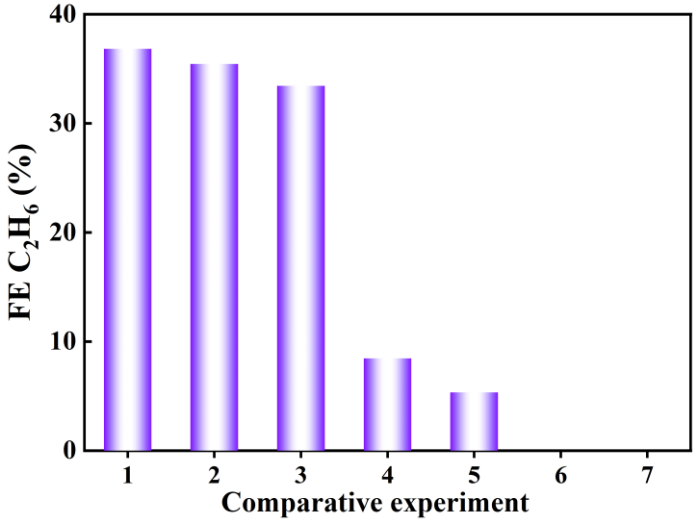

Figure S21. The FE of ethane in comparison experiments at potential of -0.53 V vs. RHE.

Table S4. The FE of ethane in comparison experiments at potential of -0.53 V vs. RHE.

No.	Comparison experiments	FE C_2H_6%
1	Standard condition	36.83
2	$PZ(CO_2)_2$ instead of PZ	35.45
3	simulated flue gas instead of CO_2	33.45
4	**M1** instead of **H1**	8.46
5	$Fe(ClO_4)_2$ instead of **H1**	5.34
6	Ar instead of CO_2	0
7	No PZ	0

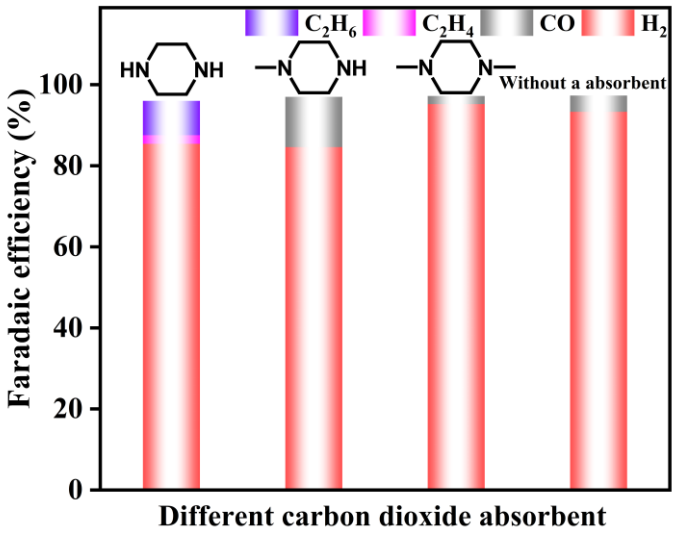

Figure S22. The Faraday efficiency of **M1** electrocatalytic carbon dioxide reduction on different carbon dioxide absorbent at -0.53 V vs. RHE under standard conditions.

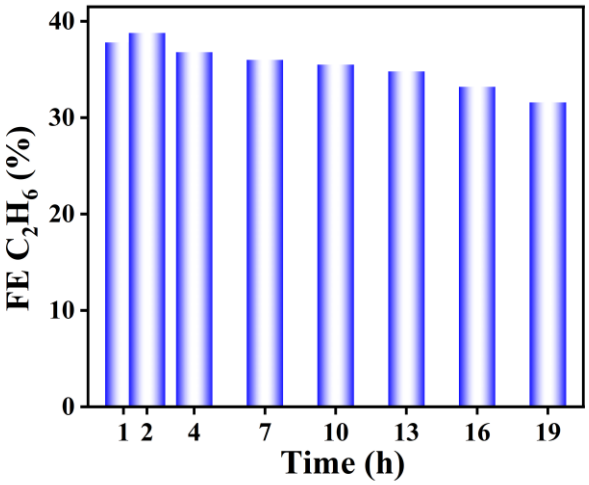

Figure S23. The Faraday efficiency (ethane) of **H1** electrocatalytic $PZ(CO_2)_2$ reduction over time at -0.53 V vs. RHE under standard conditions.

7. Detection of electrochemical CO_2RR products.

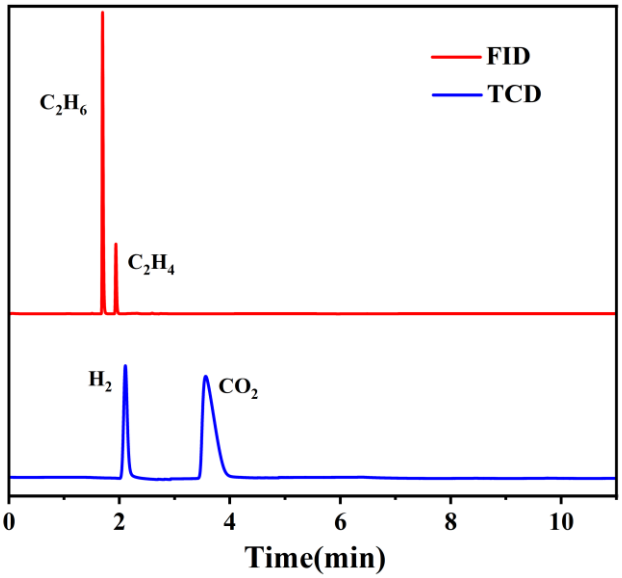

Figure S24. The GC spectra of gas products of **H1** electrolyzed for 4 h at -0.53 V vs RHE in CH_3CN/H_2O (v/v = 2:1) containing 0.1 M $LiClO_4$, 1.5 M PZ and 0.01 mM **H1**: (top) FID test results, (bottom) TCD test results. FID: detection of gaseous hydrocarbons, TCD: detection of H_2, CO_2, and CO.

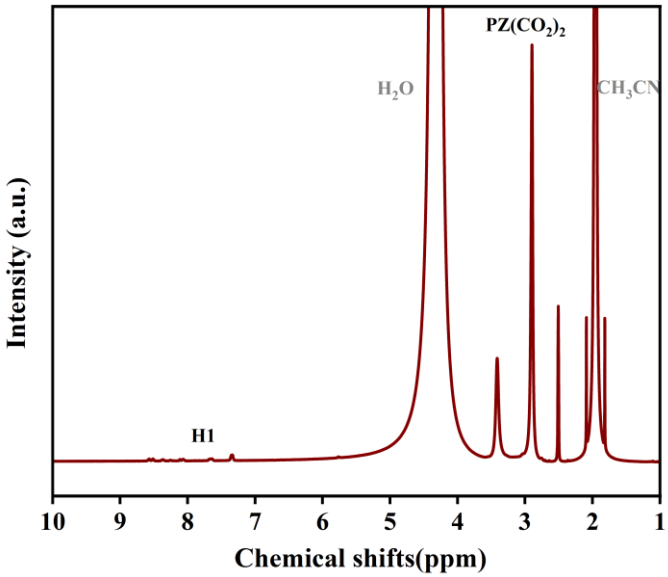

Figure S25. The ^1H NMR spectrum of liquid products of **H1** electrolyzed for 4 h at -0.53 V vs RHE in CH_3CN/H_2O (v/v = 2:1) containing 0.1 M $LiClO_4$, 1.5 M PZ and 0.01 mM **H1**. Deuterium reagent: DMSO-d_6 (2.50 ppm), 300 μL liquid products + 400 μL DMSO-d_6.

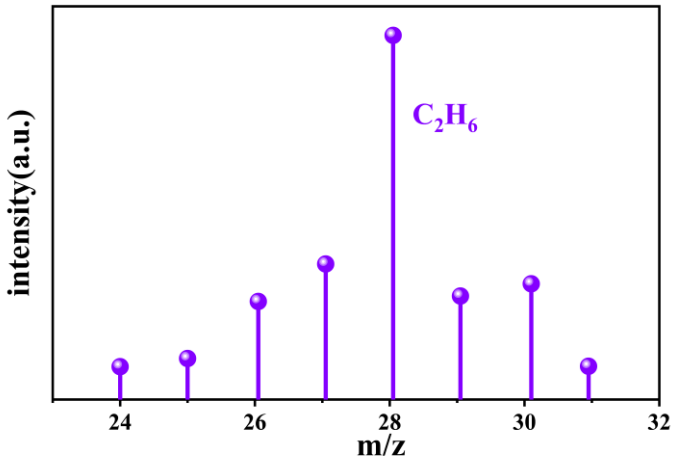

Figure S26. The GC-MS spectrum of C_2H_6 of **H1** electrolyzed for 4 h at -0.53 V vs RHE in CH_3CN /H_2O (v/v = 2:1) containing 0.1 M $LiClO_4$, 1.5 M PZ and 0.01 mM **H1**.

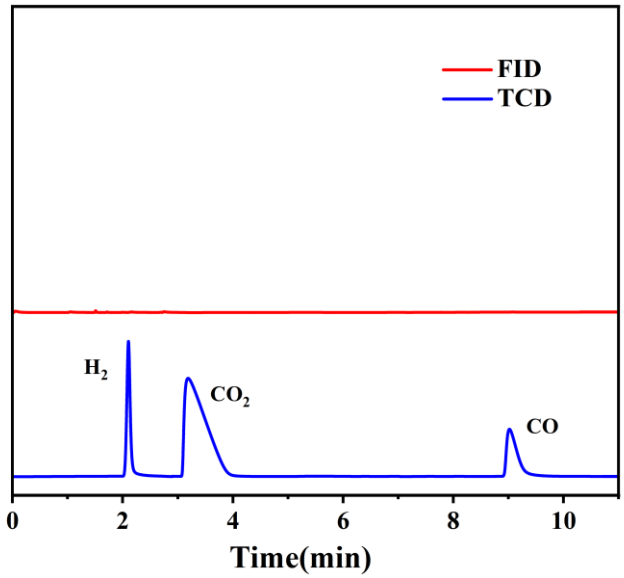

Figure S27. The GC-MS spectrum of C_2H_6 of **H1** electrolyzed for 4 h at -0.53 V vs RHE in CH_3CN /H_2O (v/v = 2:1) containing 0.1 M $LiClO_4$, 1.5 M N-methylpiperazine and 0.01 mM **H1**.

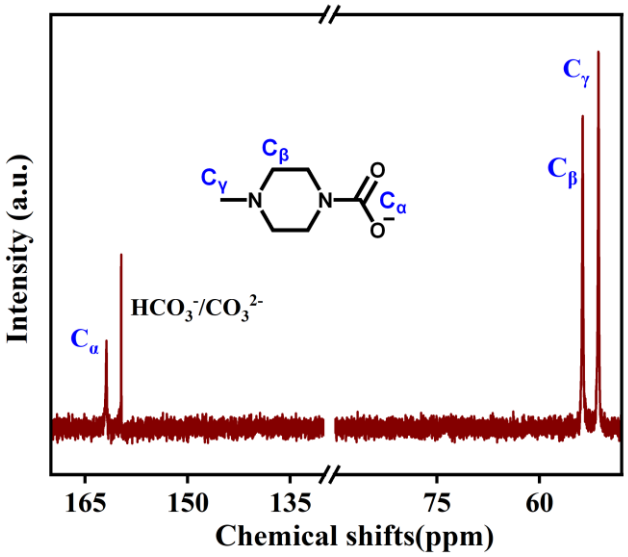

Figure S28. The ^{13}C NMR spectra of 1.0 M N-methylpiperazine solution at pH=8.0 after CO_2 absorption. The aforementioned electrocatalytic experiments were conducting at this pH.

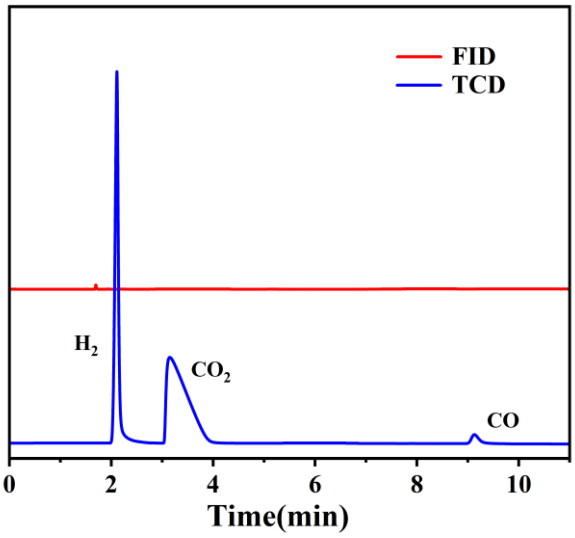

Figure S29. The GC-MS spectrum of C_2H_6 of **H1** electrolyzed for 4 h at -0.53 V vs RHE in CH_3CN /H_2O (v/v = 2:1) containing 0.1 M $LiClO_4$, 1.5 M N,N'-dimethylpiperazine and 0.01 mM **H1**.

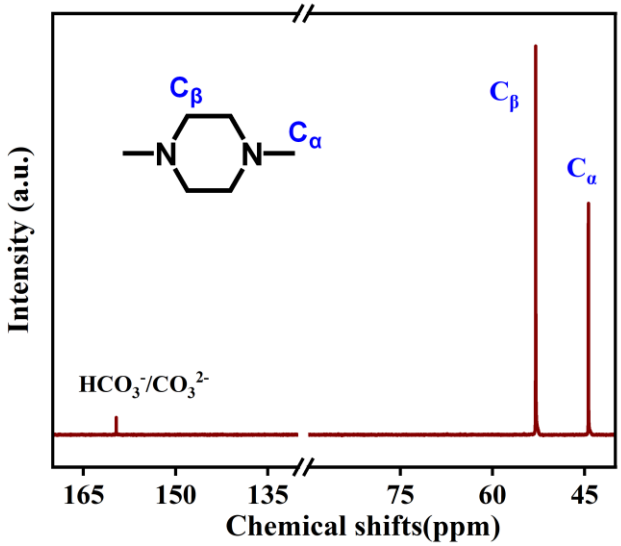

Figure S30. The ^{13}C NMR spectra of 1.0 M N,N'-dimethylpiperazine solution at pH=8.0 after CO_2 absorption. The aforementioned electrocatalytic experiments were conducting at this pH.

8. NMR spectra

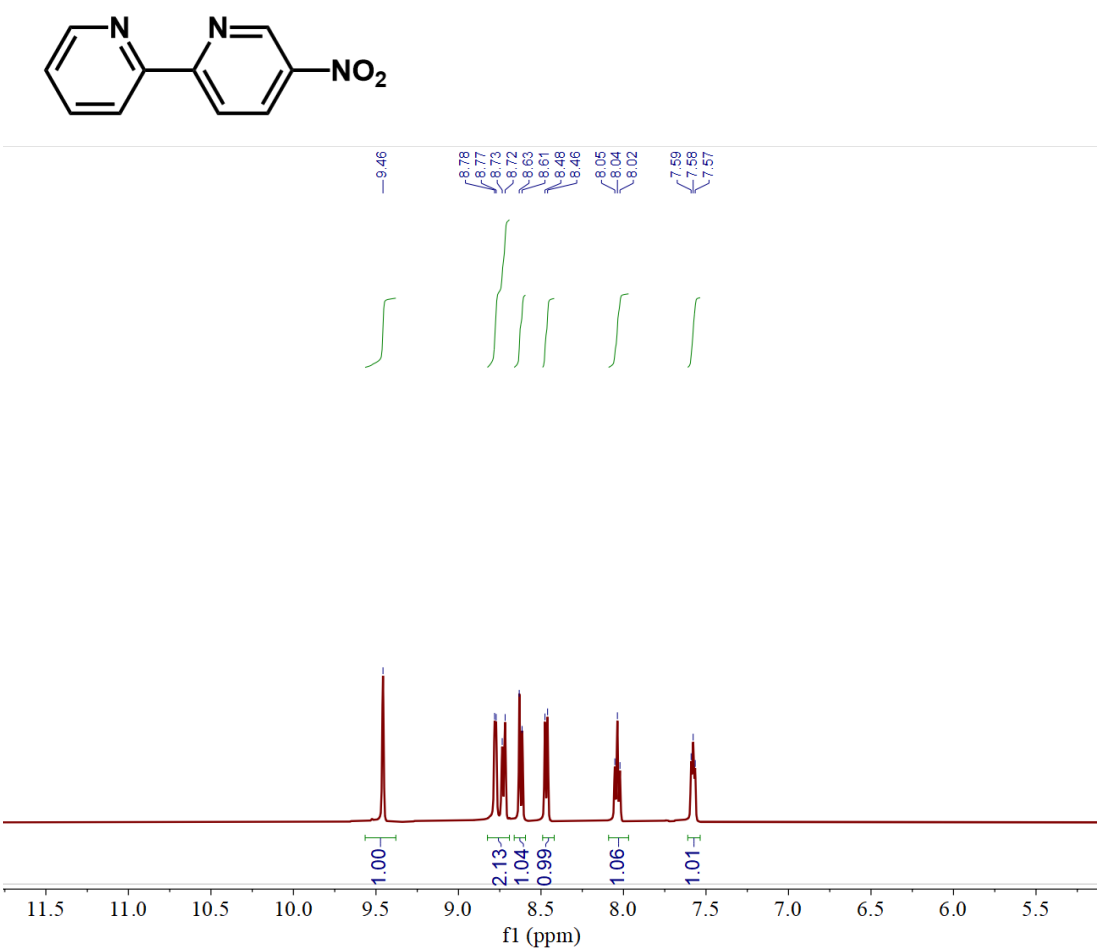

Figure S31. ^{1}H NMR spectra (500 MHz, DMSO-d_6, ppm, 298 K)) of **5-Nitroo-2,2'-bipyridine**.

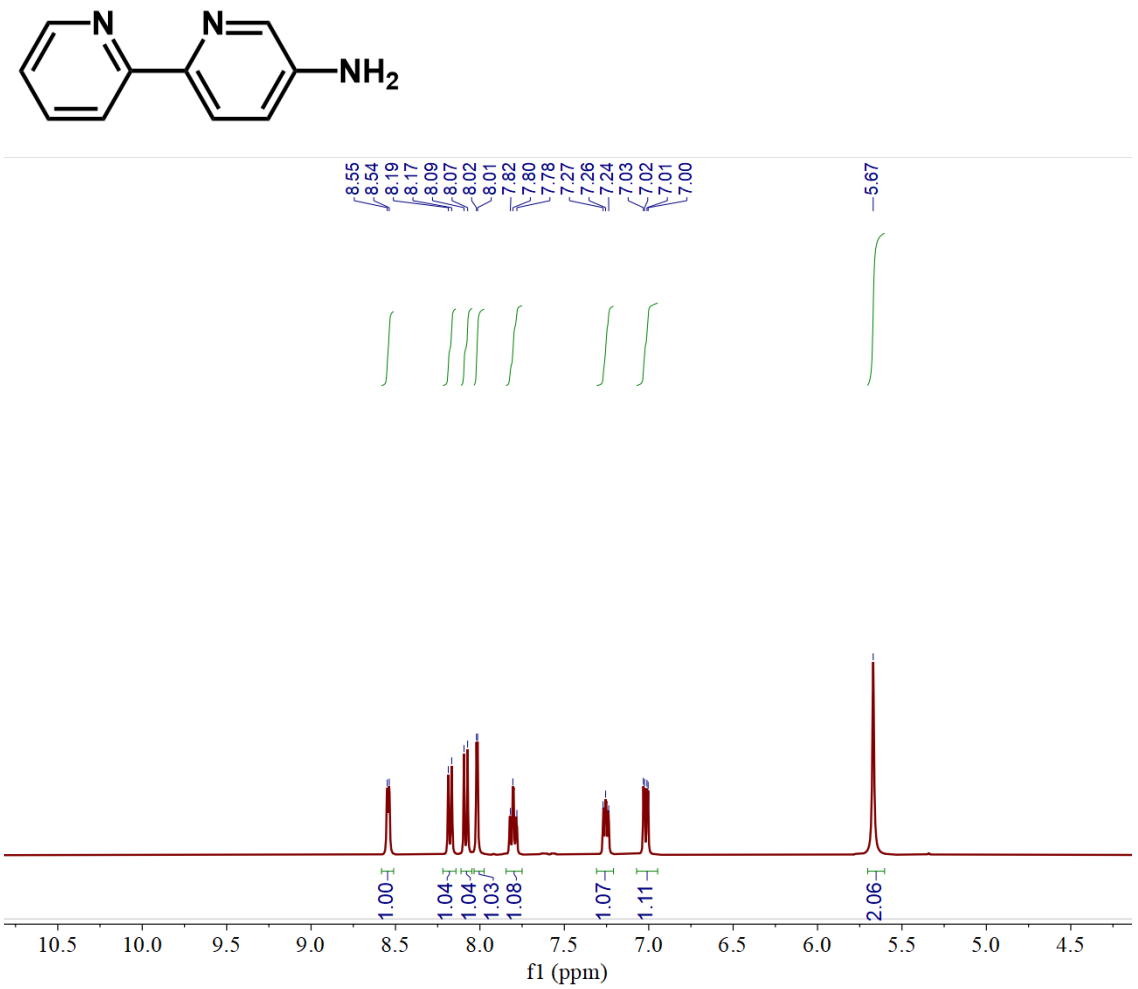

Figure S32. ^{1}H NMR spectra (500 MHz, DMSO-d_6, ppm, 298 K)) of **5-Amino-2,2'-bipyridine**.

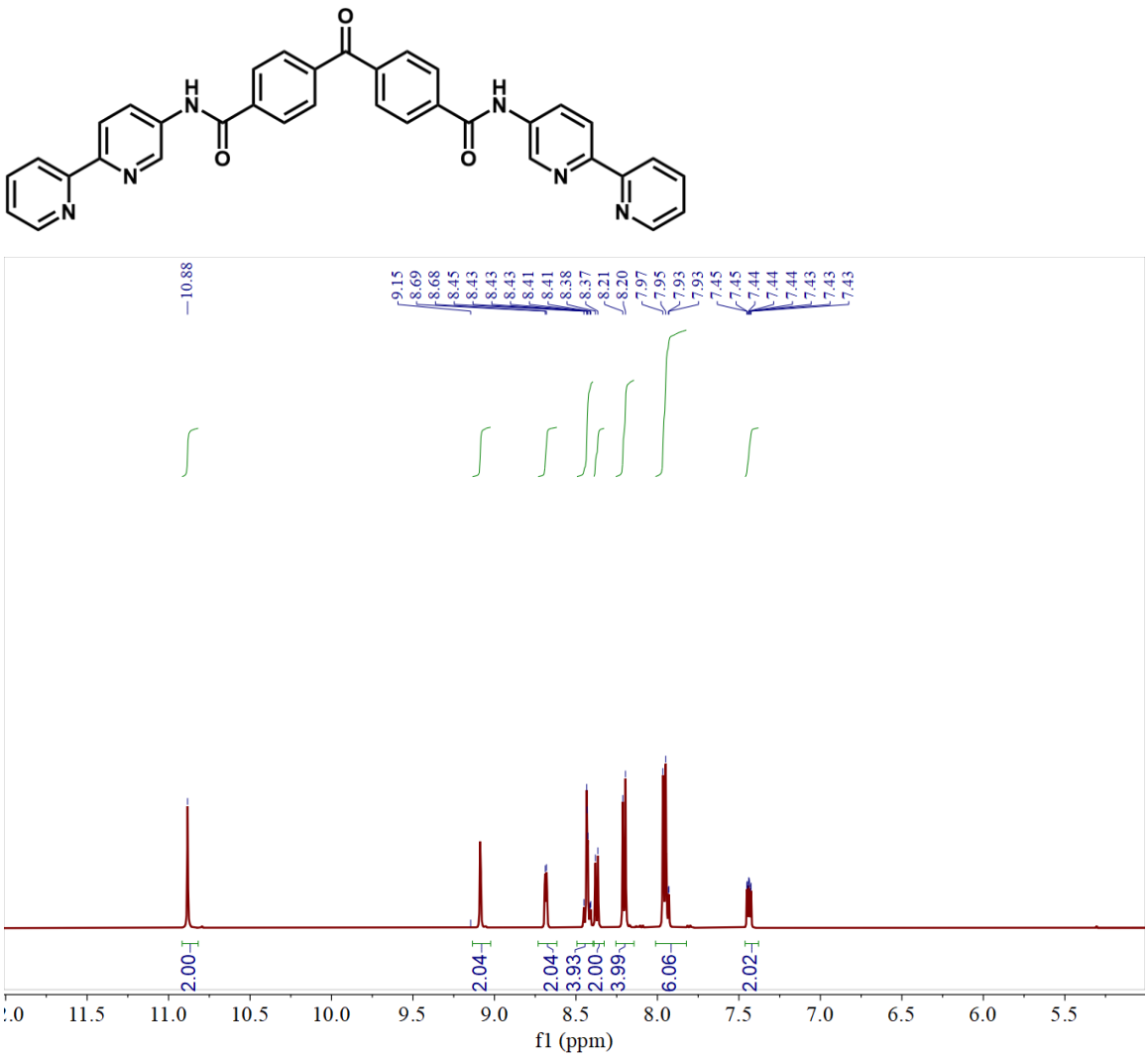

Figure S33. ^{1}H NMR spectra (500 MHz, DMSO-d_6, ppm, 298 K)) of **4,4'-carbonylbis(N-([2,2'-bipyridin]-5-yl)benzamide)**.

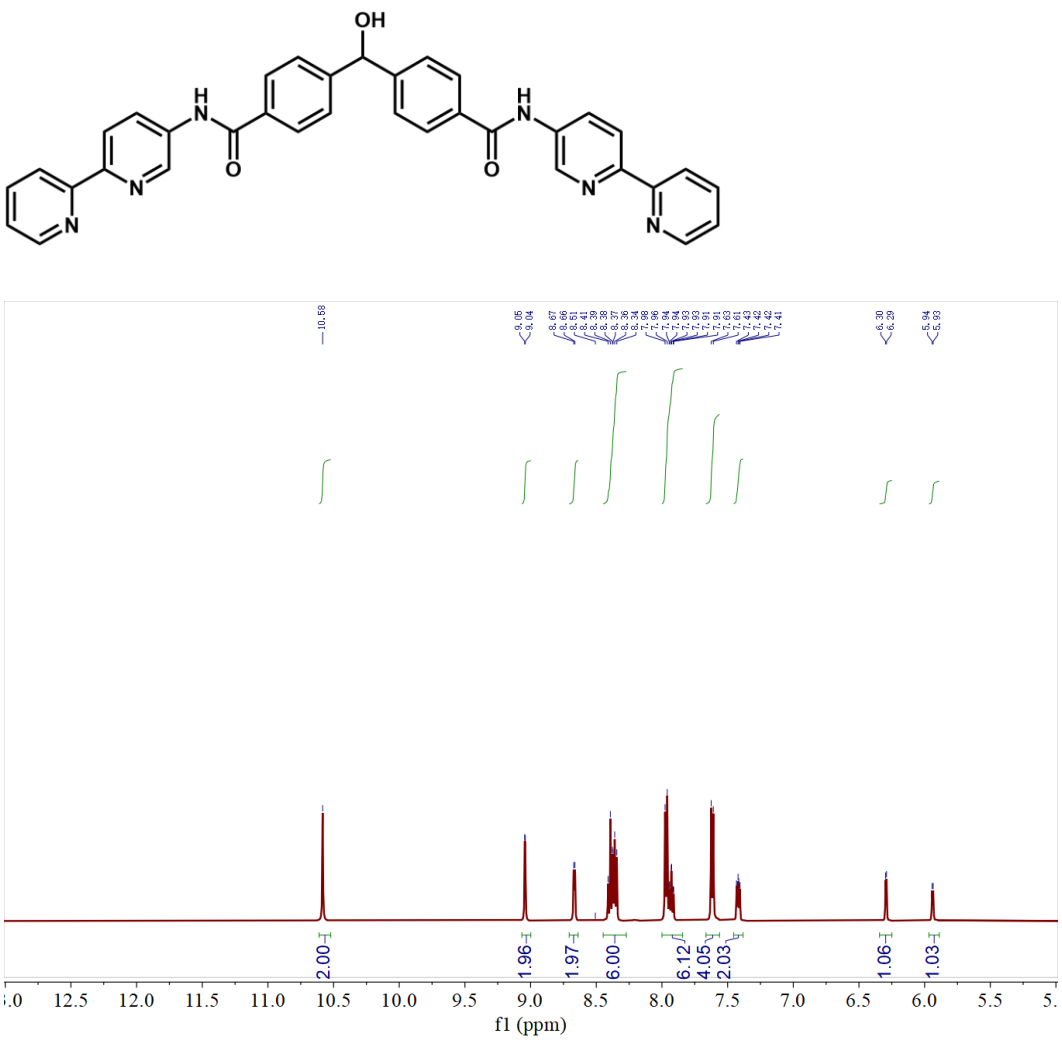

Figure S34. ^{1}H NMR spectra (500 MHz, DMSO-d_6, ppm, 298 K)) of Ligand **L**.

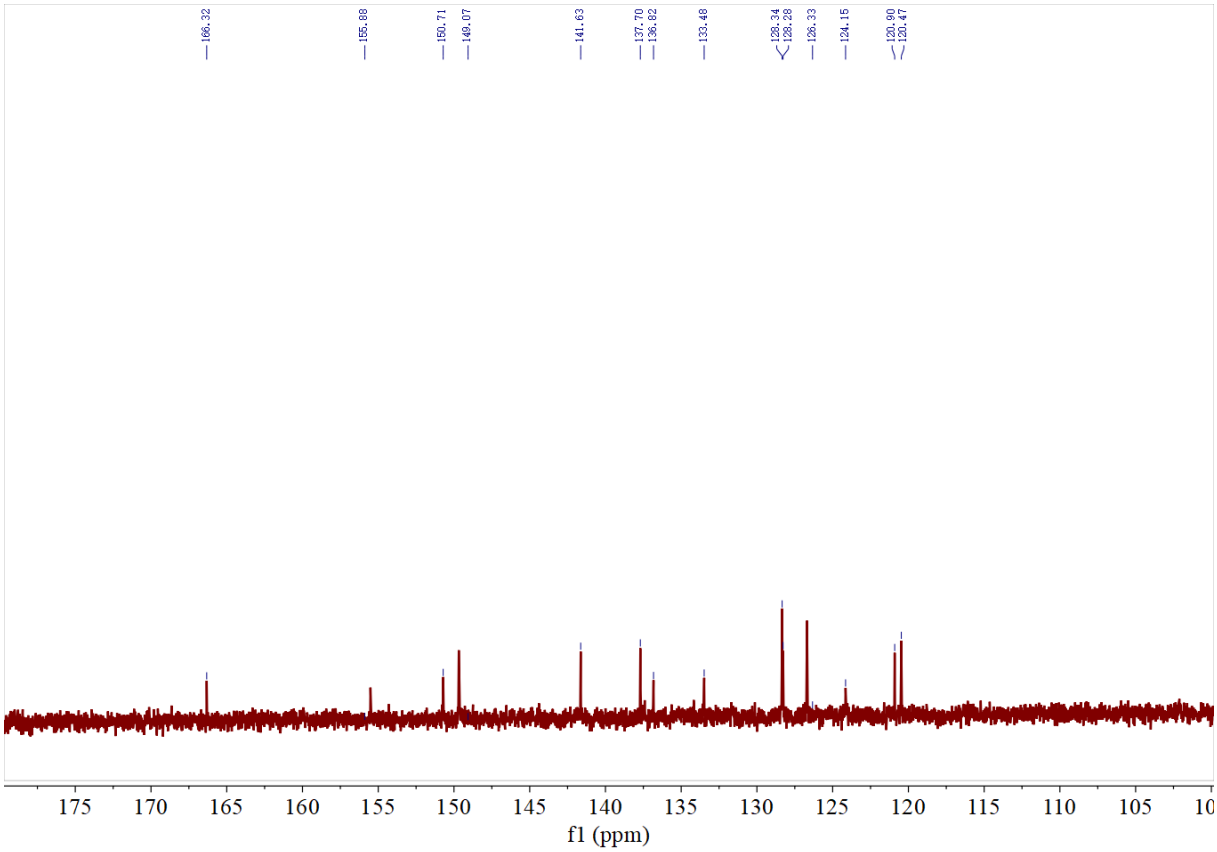

Figure S35. ^{13}C NMR (101 MHz, DMSO-d_6 ppm, 298 K) of ligand **L**.

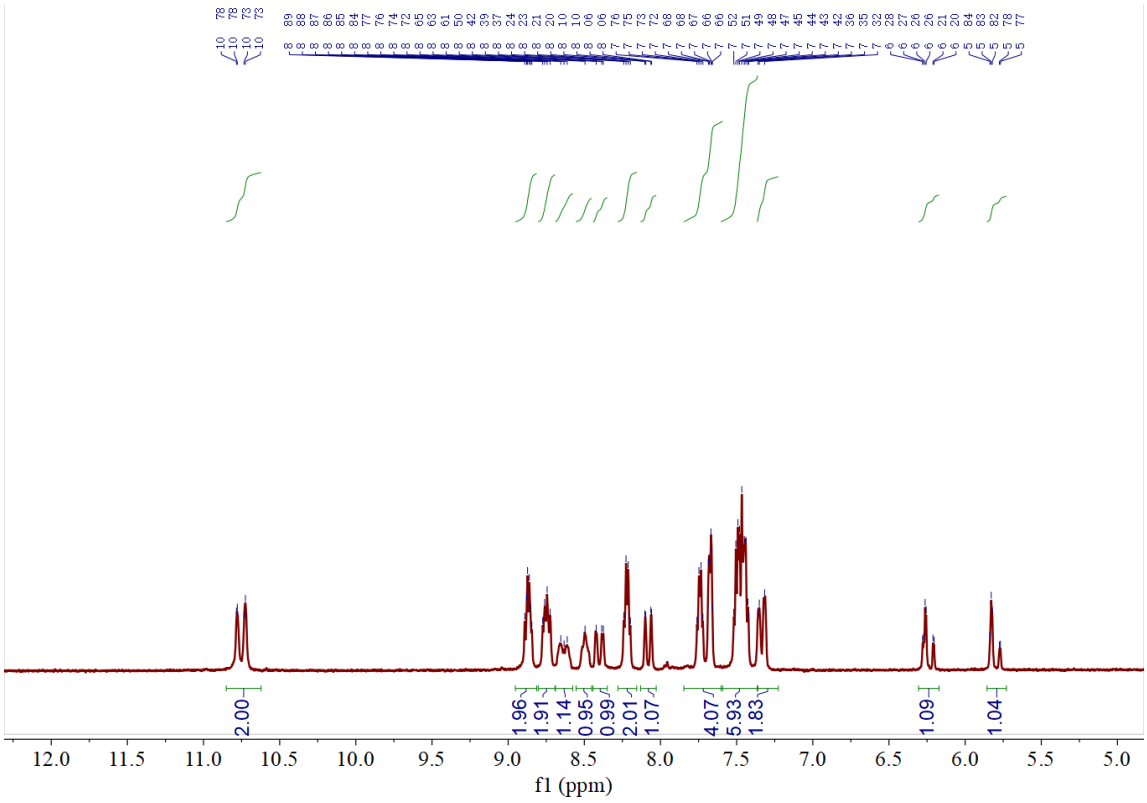

Figure S36. ^{1}H NMR spectra (500 MHz, DMSO-d_6, ppm, 298 K)) of **H1**.

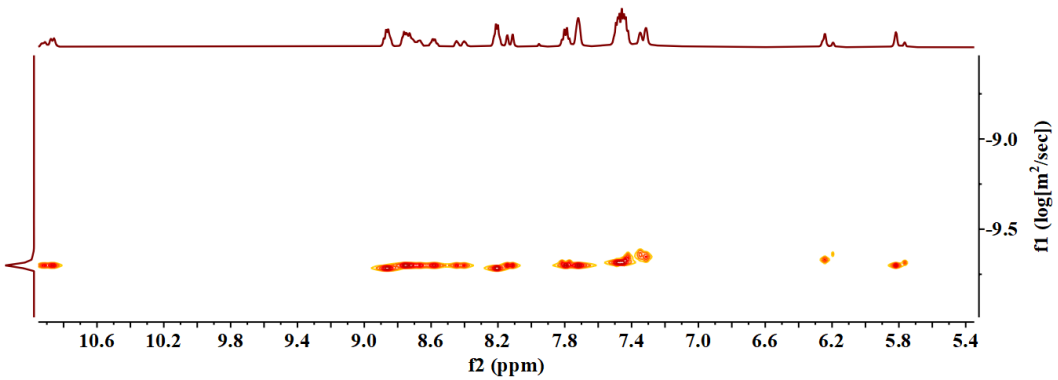

Figure S37. ^{1}H-DOSY (600 MHz, DMSO-d_6, 298 K) of **H1** (1.0 mM): D = 1.98×10^{-10} $m^2\cdot s^{-1}$**.**

8. References

1 D. Li, X. Liu, L. Yang, H. Li, G. Guo, X. Li and C. He, *Chem. Sci.*, 2023, **14**, 2237–2244.

2 Z. Wei, X. Jing, Y. Yang, J. Yuan, M. Liu, C. He and C. Duan, *Angewandte Chemie International Edition*, 2023, **62**, e202214577.

3 Y. Long, Y. Zheng, Y. Xia, L. Qu, Y. Yang, H. Xiang and X. Zhou, *ACS Catal.*, 2022, **12**, 4688–4695.

4 C. Chen, X. Yan, Y. Wu, S. Liu, X. Zhang, X. Sun, Q. Zhu, H. Wu and B. Han, *Angewandte Chemie International Edition*, 2022, **61**, e202202607.

5 Z. Wen, S. Xu, Y. Zhu, G. Liu, H. Gao, L. Sun and F. Li, *Angewandte Chemie International Edition*, 2022, **61**, e202201086.

6 P. Thordarson, *Chem. Soc. Rev.*, 2011, **40**, 1305–1323.